

# Detectability of Self-Lensing Flares of White Dwarfs with Compact Companions

GUY NIR<sup>1,2</sup> AND JOSHUA S. BLOOM<sup>1,2</sup>

<sup>1</sup>*Department of Astronomy, University of California, Berkeley, CA 94720-3411, USA*

<sup>2</sup>*Lawrence Berkeley National Laboratory, 1 Cyclotron Road, MS 50B-4206, Berkeley, CA 94720, USA*

(Dated: November 27, 2023)

## ABSTRACT

Binaries containing compact objects, if viewed close to edge on, can produce periodic brightening events under certain conditions on the masses, radii, and binary separation. Such flares are caused by one object gravitational lensing the other, in what is known as *self-lensing flares*. We present a simulation tool that efficiently reproduces the main features of self-lensing flares and facilitates a detection sensitivity analysis for various sky surveys. We estimate the detection prospects for a handful of representative surveys when searching for systems of either two white dwarfs, or a white dwarf with other compact objects, i.e., neutron stars and black holes. We find only a marginal ability to detect such systems in existing surveys. However, we estimate many such systems could be detectable by surveys in the near future, including the Vera Rubin observatory. We provide a quantitative analysis of the detectability of double-compact object self-lensing flares across the landscape of system parameters, and a qualitative discussion of survey and followup approaches to distinguish such flares from confounding events, such as stellar flares, satellite glints, and cosmic rays. We estimate 0.3, 3 and 247 double white dwarf systems could be detected by TESS, ZTF, and LSST, respectively. A similar number of systems with a neutron star or black hole companion could be detected, but we caution that the number densities of such binaries is model dependent and so our detection estimates. Such binaries can be used to constrain models of the end states of binary evolution.

## 1. INTRODUCTION

The general relativistic deflection of light passing near a massive object can lead to apparent astrometric and brightness changes, so-called gravitational lensing (Einstein 1936; Refsdal 1964). For background stars lensed by foreground compact objects in our galaxy, the multiple images of the star created during gravitational lensing are usually too small to resolve, a situation referred to as *microlensing* (Paczynski 1986). However, in many real-world cases, a brightness change with time as well as an astrometric deflection, can be observed. Such measurements can be used to find otherwise invisible compact objects such as black holes, or other dark massive objects (e.g., Bennett et al. 2002; Rybicki et al. 2018; Mróz et al. 2019; Lam et al. 2022).

Self Lensing (SL) occurs when one component in a binary system magnifies the light from the other component. In this case the magnification amplitude is typically smaller than for lensing by unrelated, distant bodies, and the time scales of the flares are much shorter: minutes or hours as opposed to days or weeks for the more typical background-foreground lensing in the Galaxy (Maeder 1973). Such systems can provide

much information on the physical properties of the binary: the orbit must be nearly edge-on for the lensing effect to be detectable, and the duration and amplitude of the flare provide constraints on the mass of the lensing body. The lensing flare is periodic, so repeat measurements can lead to determination of the orbital period. Combined with radial velocity measurements, the system parameters can be measured to high precision. To date, most binaries with compact objects, specifically neutron stars (NSs) or black holes (BHs), have been detected by the X-ray flux from accretion of gas from a close companion. Such X-ray binaries can only provide information on very close systems, that are undergoing active mass transfer. On the other hand, self-lensing systems can help shed light on a population of non-interacting, wide binaries with compact objects (Beskin & Tuntsov 2002).

The typical effective size of the gravitational effect, the *Einstein radius*, is between  $10^3$  and  $10^5$  km, depending on the orbital separation and mass of the lens. For orbits smaller than an AU, the lens is much smaller than a solar radius, so flares from main sequence stars with compact companions are hard to detect (Qin et al. 1997; Beskin

& Tuntsov 2002; Rahvar et al. 2011). Wiktorowicz et al. (2021) estimate hundreds of SL flares from MS sources (with NS or BH companions) can be detected in all-sky surveys. However, many of the flares they discuss are either very faint (with an amplitude less than 1% of the star’s light), or have a single detection during the life of the survey, so they would be very hard to distinguish from stellar flares (Kulkarni & Rau 2006) or satellite glints (Corbett et al. 2020; Nir et al. 2021a).

On the other hand, if the source is a luminous compact object, i.e., a white dwarf (WD), then the flares can become substantial, with magnifications of up to a few times the quiescent flux, even for relatively short period orbits. In some cases, X-rays from accretion on to a NS or BH can also be magnified periodically by a compact lens (D’Orazio & Di Stefano 2020).

WDs are therefore favorable sources for detection of SL flares, albeit with a smaller total number of observable systems compared to MS sources. In cases where the compact object is a NS or BH, the temporal behavior and brightness of the flare is determined by the size of the Einstein radius and the finite size of the source. For a WD lens occulting a WD source, the physical size of the lens must also be taken into account. In such cases the shape of the lightcurve would be determined by a competition between the lens magnification and the physical occultation by the lens (e.g., Kasuya et al. 2011; Han 2016).

Binaries with wide orbits (on the order of AUs) typically produce brighter flares. Close orbits (with semimajor-axis  $a < 10^{-2}$  AU) would produce faint flares (on the order of few percent increase in flux), with minute-scale durations. While detection of such short, faint flares is challenging, such systems would have short periods (on scales of hours), and so would be easier to follow up and verify.

Self-lensing binaries are rare and hard to detect. The system must be close to edge-on, and the flare occurs only within a small fraction of the orbit (low duty cycle). Double White Dwarf (DWD) systems are fairly common, where the fraction of WDs in a binary is 0.1–1, depending on the separation (Toonen et al. 2017; Maoz et al. 2018). However, the probability of finding a DWD with a sufficiently large inclination angle (i.e., almost edge on) significantly reduces the number of observable systems, especially when considering wider orbits with  $a = 10^{-2}$ – $10^{-1}$  AU.

NS and BH companions to WDs are expected to be even rarer, given the steep mass distribution of stars (Wiktorowicz et al. 2019). In this case, however, the higher mass and smaller physical size of the lensing object may make them detectable at closer orbits, which

means more systems will be sufficiently inclined to have visible flares. The shorter periods would also give such systems a higher duty cycle and shorter flare repeat time, making them easier to detect and follow up. It should be noted that WDs in binaries with pulsars (fast spinning NSs) have been identified Istrate et al. (2014); Adamane Pallathadka et al. (2023).

Beskin & Tuntsov (2002) estimated up to 22 WD-WD pairs and up to 16 WD-BH pairs can be detected using the same telescope as was used by the Sloan Digital Sky Survey (SDSS; York et al. 2000). Masuda & Hotokezaka (2019) and Chawla et al. (2023) discussed the prospects of finding black holes using the self-lensing signal, among other indicators such as ellipsoidal variation and relativistic beaming.

All-sky surveys increasingly push the boundaries of sky coverage, cadence, and photometric precision. The Zwicky Transient Facility (ZTF; Bellm et al. 2019), The All-Sky Automated Survey for Supernovae (ASAS-SN; Shappee et al. 2014), and the future Vera Rubin Legacy Survey of Space and Time (LSST; Ivezić 2007; Ivezić et al. 2019) have large fields of view (multi-square degree) and cadence from few-per-night to once-per-few-nights. The Dark Energy Camera (DECam; DePoy et al. 2008) conducts multiple surveys, including a Deep Drilling Fields survey that takes multiple images of the same fields over multiple, consecutive nights with LSST-like depth (Graham et al. 2023). Space telescopes such as the Transiting Exoplanet Survey Satellite (TESS; Ricker et al. 2014), and the future Cubesats for Rapid Infrared and Optical Surveys (CuRIOS; Lu et al. 2022) will observe large fractions of the sky continuously at high cadence and high photometric precision, while similar efforts to provide continuous imaging of large fields of view every few seconds are also planned and ongoing, e.g., the Weizmann Fast Astronomical Survey Telescope (W-FAST; Nir et al. 2021b) the Large Array Survey Telescopes (LAST; Ofek & Ben-Ami 2020), the Evryscope (Ratzloff et al. 2019) and the Argus Optical Array (Law et al. 2022).

Since each such survey has dramatically different cadence, field of view, depth and precision, we present in this work a detailed analysis of the detection probability to find self-lensing flares from different types of binaries, given the properties and observing strategy of each survey. Using simple models for the distributions of mass, temperature, and binary separations of WDs with other WDs or more massive compact objects, we estimate the expected number of detections of self-lensing systems in various surveys. The simulations described in this work can be repeated (for the given surveys, or by defining

other survey parameters) using an open source software package.<sup>1</sup>

We discuss the details of the simulation tools used to produce the self-lensing flares in §2. We present the physical properties of self-lensing systems in §3 and survey the landscape of the parameter space of such systems in §4. We discuss the interplay of astronomical surveys’ properties in regards to the chances of detection of self-lensing flares in §5. We present the results of the simulations, including each survey’s ability to detect self-lensing flares in §6. We discuss these results, and compare them to other cases of self-lensing systems and eclipsing systems in §7. We conclude in §8.

## 2. SELF-LENSING SIMULATOR

Light is deflected around massive objects and can be focused by a point mass in such a way that amplifies the amount of light reaching an observer. A point source close to such a massive object (“lens”), would be seen as two images. The positions of each image are given by the lens equation (Paczynski 1986; Beskin & Tuntsov 2002):

$$u = d - \frac{1}{d}, \quad (1)$$

where  $u$  and  $d$  are the normalized distances (on the plane of the sky at the distance to the lens) from the center of the lens to the center of the source, and from the center of the source to the center of its images, respectively. These two sizes are both given in units of the Einstein radius:

$$R_E = \sqrt{\frac{4GM(D_S - D_L)D_L}{c^2 D_S}} \approx \sqrt{\frac{4GMa}{c^2}} \quad (2)$$

where  $D_S$  and  $D_L$  are the distances to the source and lens, respectively, the mass  $M$  is of the lens, and  $G$  and  $c$  are the usual gravitational constant and speed of light. The approximation above holds when the lens is orbiting the source at a distance  $a \ll D_S \sim D_L$ . For  $M$  in units of a Solar mass, and  $a$  in AU, the Einstein radius is  $R_E \approx 1.5 \times 10^4 \sqrt{Ma}$  km. We will assume a circular orbit in all calculations, so  $a$  can also be referred to as the semimajor axis.

If the lens and source are perfectly aligned,  $u \rightarrow 0$  and we get a ring around the source position, with a radius given by the Einstein radius, from Equation 2. If the lens is not perfectly aligned we get two images with positions that can be found by solving Equation 1:

$$d_{1,2} = \frac{1}{2} \left( u \pm \sqrt{u^2 + 4} \right). \quad (3)$$

If the Einstein radius is much larger than the source, we can approximate the resulting lightcurves as point source events (e.g., Paczyński 1986; Rybicki et al. 2018):

$$A = \frac{u^2 + 2}{u\sqrt{u^2 + 4}}, \quad (4)$$

where  $A$  is the magnification of the source given the source-lens distance  $u$ .

For a source of finite extent, Equation 3 can be used to find the image of the contour tracing the edges of the source. If the lens is inside the source area, we get two warped contours, one inside the other. The source is magnified and warped and has a hole inside where light is deflected away from the observer. If the lens center is outside the source region, the contours are separated, one inside the Einstein radius and one outside of it. We show three representative configurations in Figure 1.

The surface brightness of the source is preserved in the image(s), but the surface area is larger than the area of the source, such that the total amount of light is magnified when the lens passes near the source. Since in most cases the images are not symmetrical, there is also an offset of the center of light from the true source position. Thus, the effects of microlensing, even when the images cannot be resolved, can be detected either in photometric or astrometric measurements.

We turn to estimating the magnification and offset for each value of  $r_s = R_s/R_E$ , the normalized source size, and  $u$  (the normalized separation of source and lens centers). For each geometry we draw a circular contour of size  $r_s$ , and map the points, using Equation 3, unto a digital binary image matrix. The result is an outline for two shapes. Inside the contours we set the binary image to one, and outside the contours to zero. For geometries where  $u < r_s$  the shapes are one inside the other, so we subtract the small one from the big one (using a xor operation). In geometries where  $u > r_s$ , the images are separate and we calculate the results for each one separately.

In these binary images, the relative area represents the total flux, while the first moment gives an estimate of the astrometric offset. If the binary map is given by  $I$  and one of the image coordinates is given by  $x$ , then the flux  $f$  and moment  $m$  are given by

$$f = \sum I, \quad m = \frac{\sum xI}{f}. \quad (5)$$

Example magnification curves, as a function of distance between lens and source, for several source sizes, are shown in Figure 2.

Self-lensing objects often have an Einstein radius on the order of a few thousands of km, similar to the size

<sup>1</sup> [https://github.com/guynir42/self\\_lens](https://github.com/guynir42/self_lens)

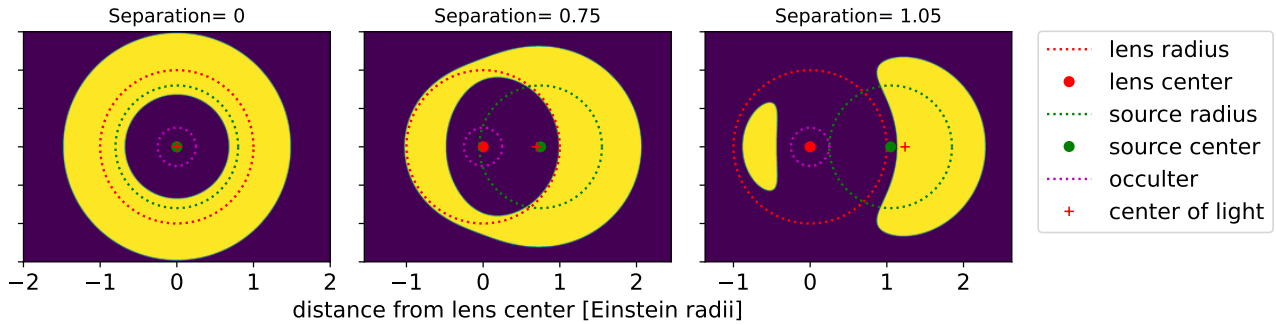


**Figure 1.** Examples of configurations of microlensing by a source with size 0.8 Einstein radius units. Left: the lens and source are aligned. Middle: the lens is offset but still inside the source area. Right: the lens is outside the source. The dark purple is outside the contours of the lensed image (no light) and the bright yellow is inside the contours (light imaged from the source surface).

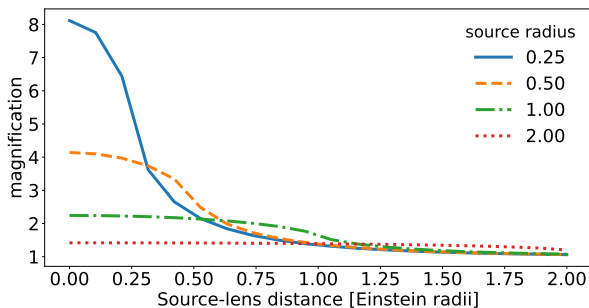


**Figure 2.** Magnification as a function of distance between lens and source centers (on the image plane). Several sizes of the source are shown, in units of Einstein radius. The smaller sources are more magnified, but their magnification drops off faster with separation.

of planets or WDs. This leads to strong finite source effects when the source is a WD or a main sequence star. When the lensing object is also a WD, its size could be close to, or even larger than the source and the Einstein radius, leading to substantial eclipses at the same time that the source is magnified by the lens (Beskin & Tuntsov 2002; Han 2016). Adding this effect to our calculations is simple: we subtract the region of the physical extent of the lens, given by the radius  $r_L = R_L/R_E$ , normalized to the Einstein radius, from the binary image  $I$  before calculating the flux and offsets for each geometry. Thus, we can calculate the flux and offset for any self-lensing geometry, characterized by the three parameters:  $u$ ,  $r_S$  and  $r_L$ . Magnification curves for a constant source size but for various occulter sizes are shown in Figure 3. In the case where the occulter is much larger than the source (1.2 vs. 0.5 Einstein radii)

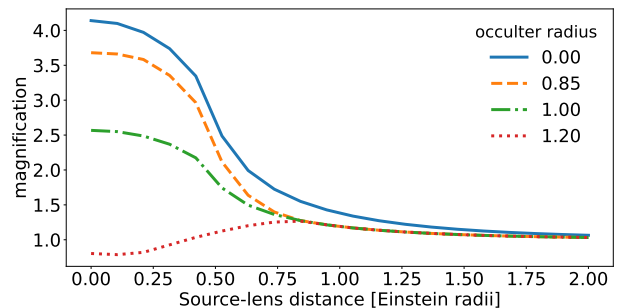


**Figure 3.** Magnification as a function of distance between lens and source centers (on the image plane). Several sizes of the physical occulter are shown, in units of Einstein radius. The source in this example has a size of  $0.5 R_E$ . When the occulter is bigger than the source ( $0.85$ – $1.00 R_E$ ) the lensing flare is somewhat weakened. When the occulter is substantially larger than the source ( $1.2 R_E$ ) the flare is completely lost, and replaced with an eclipse.

the flare is completely suppressed and replaced by an eclipse.

In Figure 4 we show the astrometric offset of sources of different sizes at various lens-source distances. The shifts are generally limited to a fraction of an Einstein radius. It should be noted that, for self-lensing systems, with lens mass of  $\sim M_\odot$  and semimajor axis of  $\sim 1$  AU, the Einstein radius is about  $10^{-4}$  AU. At a distance of 100 pc an offset of one Einstein radius would be equivalent to a micro-arcsecond of astrometric offset. Thus we conclude that self-lensing systems would have undetectable astrometric offsets.

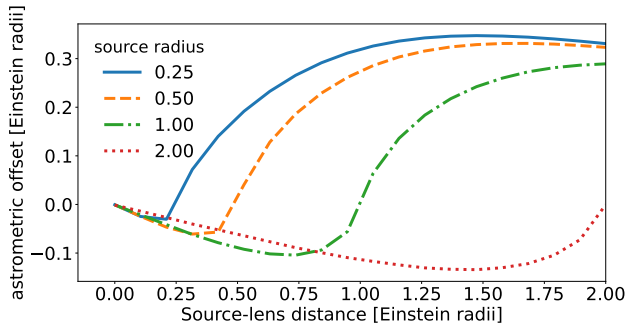


**Figure 4.** Astrometric offset as a function of distance between lens and source centers (on the image plane). Several sizes of the source are shown, in units of Einstein radius. The offsets reach a fraction of an Einstein radius, which, for typical values of self-lensing systems, would be about  $10^{-4}$  AU, which is under a micro-arcsecond for systems at a distance of 100 pc.

**Table 1.** Pre-calculated datasets

Source radii	Distances	Lens radii	Step sizes
0.01 – 0.1	0.0 – 3.0	0.0 – 2.0	0.005
0.1 – 1.0	0.0 – 10.0	0.0 – 5.0	0.025
1.0 – 5.0	0.0 – 20.0	0.0 – 10.0	0.1

NOTE—All sizes are relative to the Einstein radius  $R_E$ . Step sizes for these datasets are uniform across the grid in all three parameter axes.

This method of calculation is quite computationally slow.<sup>2</sup> To facilitate faster analysis we pre-calculate the relevant values over a grid of parameters, and use them to interpolate the results in between the grid points. In this work we utilized three pre-computed datasets, each covering a different range of parameters. These parameters are summarized in Table 1.

For sources smaller than those available in the first dataset, i.e.,  $r_S < 0.01$ , we use the point source approximation given by Equation 4. For sources further away than the maximal distance, we also use the point source approximation, with the assumption that at  $u \gg r_S$ , each point on the source has a similar distance to the lens, so that the total magnifications is given by the same approximation. At these distances, the lensing effect yields only small magnifications (less than 1%), so

<sup>2</sup> On an Intel i7-9850H, calculating a lightcurve for a single system, including multiple geometries where the lens moves across the source, can take several seconds.

the exact choice of approximation does not affect our calculations in a major way. For sources larger than those in the last dataset, we use the solution of Agol (2003), using elliptical integrals.

For each dataset, we only save the difference in flux and un-normalized moment, between geometries with adjacent source sizes. These results represent the fluxes and moments that would be measured for an annulus with uniform surface brightness. The reason we keep the results in this way, rather than store the results for disks of uniform brightness, is to be able to reconstruct the magnifications and offsets for different limb-darkening profiles. With a different relative surface brightness of each radius on the source disk, we can sum the contributions to the flux and moment for each annulus, using appropriate weighting, and produce a result for an arbitrary darkening profile. To recover the results for uniform disks, we simply sum the results of all annuli with equal weights.

### 3. PHYSICAL PROPERTIES OF SELF-LENSING SYSTEMS

The lensing flare would appear different for various types of binary components. The source must be a luminous source, so it could be a main sequence or giant branch star (MS or GB) or a white dwarf (WD). In this work we do not address the MS/GB options, as the stars are substantially larger than WDs, and the signal would be diluted by a large factor unless considering very long orbits. Even for MS sources that have detectable flares, e.g., for small stars with wide orbit companions (yielding large Einstein radii), the signal would be swamped by false alarms from stellar flares. To simplify the search we focus on WD sources.

The lens must be compact in order to generate a positive signal, so white dwarfs, neutron stars or black holes are the possible lenses. The WD case is particularly challenging since the size of the physical object is often comparable to the Einstein radius, so the signal is composed of a lensing flare superimposed on an eclipse dip. For NS or BH lenses, we assume the physical size of the lens is negligible and calculate only a positive flare. We simulate lenses of three types, with non-overlapping mass ranges: WDs have  $0.2M_\odot < M_{\text{lens}} < 1.2M_\odot$ , NSs have  $1.2M_\odot < M_{\text{lens}} < 2.5M_\odot$  and BHs have  $2.5M_\odot < M_{\text{lens}} < 30M_\odot$ . It should be noted that in all our simulations and results, there is no difference between a NS and a BH, and they are treated as identical objects with different masses.



We assume the radius of a WD is given by Equation 5 of Beskin & Tuntsov (2002) (see also Nauenberg 1972):

$$R_{\text{WD}} = 0.01125R_{\odot} \left[ \left( \frac{M_{\text{WD}}}{1.454M_{\odot}} \right)^{-\frac{2}{3}} - \left( \frac{M_{\text{WD}}}{1.454M_{\odot}} \right)^{\frac{2}{3}} \right]^{\frac{1}{2}}. \quad (6)$$

Another free parameter that determines the system properties is the spatial distance between source and lens: the semimajor axis,  $a$ . The orbits we consider here are  $10^{-2} \leq a \leq 10$  AU for WD-WD binaries and  $10^{-4} \leq a \leq 1$  AU for the WD-NS and WD-BH binaries. As a reference, two WDs with masses of  $0.6 M_{\odot}$  at an orbit of  $a = 10^{-2}$  have a period of 8 hours. For  $a = 10^{-3}$  the period is 15 minutes, and for  $a = 10^{-4}$  the period is 30 s. For one such WD orbiting a  $30 M_{\odot}$  BH at a semimajor axis of  $a = 10^{-4}$  the orbital period is about 6 s. It should be noted that systems with  $a = 10^{-4}$  AU will have a typical decay time due to gravitational radiation (Brown et al. 2016) on the order of a few years, or a few days, for a  $0.6 M_{\odot}$  WD with a  $1.5 M_{\odot}$  NS or a  $30 M_{\odot}$  BH, respectively. Since such systems are expected to be very short lived, we do not expect to detect such systems.

Although tighter orbits are physically allowed by the sizes of the objects, the smaller distances correspond to small Einstein radii, so the shortest period systems would be undetectable in most cases.

The maximal semimajor-axes we consider in this work are 10 AU for WD-WD and only 1 AU for the other binaries. Beyond 1 AU the fraction of systems seen edge on, and the duty cycle of such systems, both decrease substantially. In addition, following up such systems with periods on the order of a year becomes very difficult, so even if such a system is ever seen, it will most likely never be correctly identified.

The temperatures of the WD sources, and lenses in the case of WD-WD systems, have a strong effect on the detectability of the system. Hotter WDs will be brighter and can be detected at larger system-observer distance than cool ones. If the system is a double WD, the amount of dilution the flare of the lensed WD suffers from the light of the lensing (non-lensed) WD is determined by the size and temperature of each component. The range of possible temperatures we use is  $4000^{\circ}\text{K} \leq T_{\text{WD}} \leq 32000^{\circ}\text{K}$ , which is similar to the range of values in the sample presented by Gentile Fusillo et al. (2021). We assume the number of observable WDs with temperatures above  $32000^{\circ}\text{K}$  is small, and does not change our results substantially.

We assume all systems follow circular orbits. This may be a good approximation for close binaries that have undergone common envelope evolution, and even

in cases where the eccentricity is non-negligible, it has only a mild effect on the resulting flare. The exact distance and velocity of the lens at the time when it crosses near the line of sight of the source would be different by some small factor from the values we used here, with the assumption of a circular orbit. This can make the flare duration and size somewhat different from our simulations. But, since we are mostly interested in the average properties, we choose not to add the additional parameters required to simulate eccentric orbits, which saves a large computational cost.

In addition to the self-lensing optical signal, we also calculate the gravitational wave (GW) strain expected to be emitted from each binary in the simulation. The strain is given by:

$$h_{\text{GW}} = 4 \frac{(GM)^{5/3} (\pi f)^{2/3}}{D_L c^4}, \quad (7)$$

where  $\mathcal{M} = (M_s M_l)^{3/5} / (M_s + M_l)^{1/5}$  is the chirp mass,  $f = 2/P$  is the GW frequency calculated from the binary orbital period  $P$ , and  $D_L$  is the luminosity distance (in case of Galactic binaries, this is simply the distance to the system).

For self-lensing DWD binaries, this strain is well below the LISA noise level (Smith & Caldwell 2019). This is in contrast to eclipsing WD-WD binaries that have much closer orbits and are excellent targets for LISA (e.g., Burdge et al. 2019; Coughlin et al. 2020; Burdge et al. 2020). Short-period binaries with a NS or BH would be able to generate a detectable signal. Such measurements would provide additional constraints on the parameters of the system, or, conversely, could be used to narrow down the search for close binaries, if such systems are first detected by LISA at a distance where wide-field surveys cannot blindly detect the photometric variability. A plot of the expected LISA sensitivity, compared to a range of DWD, WD-NS and WD-BH systems and the expected strain they would produce at a distance of 1 kpc is shown in Figure 5. We see that only massive WD-BH binaries have a chance of being detected in both photometric surveys and space-based GW detectors.

#### 4. SELF-LENSING PARAMETER SPACE

Some example simulated systems are shown in Figures 6–9. We show the resulting lightcurves in a time range close to the time of the flare (not the entire period, which is usually much longer than the flare duration). Note that at different masses and orbits the typical time scales and magnifications can vary dramatically. The parameters for each systems are noted in two boxes overlaid on the plot. These include, among other information, the inclination  $i$ , which is defined as edge

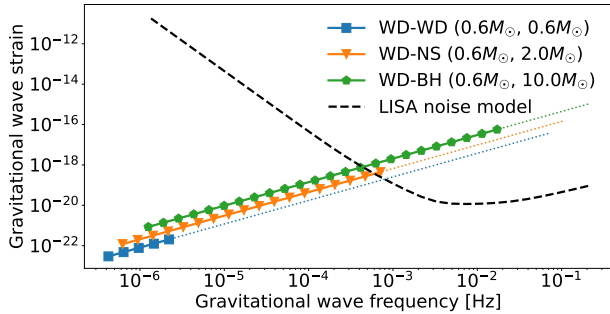


**Figure 5.** The expected gravitational strain, compared to the nominal LISA noise model, (given by Smith & Caldwell 2019). The DWD systems have equal mass of  $M_l = M_s = 0.6 M_\odot$ . The WD-NS system has masses of  $M_s = 0.6$  and  $M_l = 2.0 M_\odot$ . The WD-BH system has masses of  $M_s = 0.6$  and  $M_l = 10.0 M_\odot$ . All systems are placed at 1 kpc from the observer, and we assume they are observed over 4 years of the LISA life time. The solid lines represent systems have peak self-lensing flare amplitudes above 10%. The dotted lines show additional systems with lower orbits and stronger GW emission, that have self-lensing flares below the 10% level, and are harder to detect photometrically. The dashed line is the LISA noise model. We see that only the WD-BH systems can be detected easily by both photometric all-sky surveys, and space-based GW detectors.

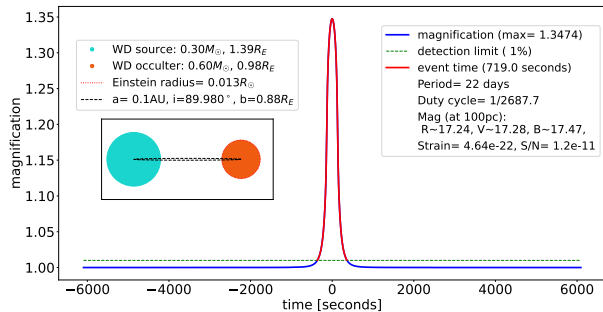


**Figure 6.** A simulated WD-WD system. The main plot shows the magnification as a function of time, while the inset shows a cartoon of the system (not to scale). The masses of the stars are 0.3 and  $0.6 M_\odot$ . The orbital radius is 0.1 AU, giving a 22 day orbit. The larger and less massive WD is lensed by the smaller and more massive companion. The flare duration is about 700 s, with a duty cycle of about 1/2700. The maximum magnification of 1.35, along with the flare duration, makes this an easy target to detect. The low duty cycle and long period, however, will make it very hard to identify such a system. The gravitational strain of this system, of  $h \approx 10^{-23}$  is too weak to be detectable by, e.g., LISA.

on when  $i = 90$ , and the impact parameter  $b$ , which is the on-sky distance between lens and source centers at the point of closest approach.

As discussed above, the different parameters of each binary have different and interacting effects on the de-

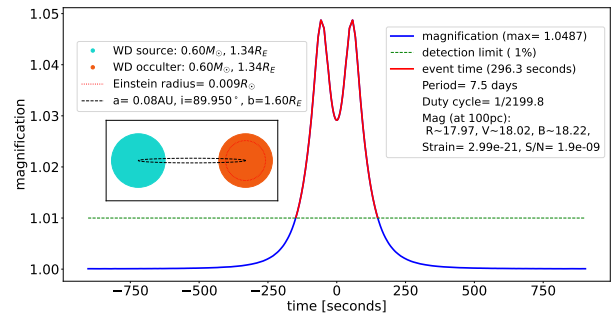


**Figure 7.** A simulated WD-WD system with a visible eclipse. The plot is similar to Figure 6 but with conditions that favor an eclipse in the middle of the lensing flare. The masses of the stars are both  $0.6 M_\odot$ , such that the source is smaller than the previous example shown in Figure 6. The orbital radius is 0.08 AU, which also reduces the Einstein radius relative to the previous example. The increased source mass and closer orbit give a period of only 7.5 days. The physical size of the occulting WD is seen to reduce the magnification during the middle part of the flare. The flare duration is about 300 s, with a duty cycle of about 1/2200. Since this system is symmetric, the period would be halved and the duty cycle doubled, compared to the parameters shown here. The maximum magnification of only 1.05, already makes this a challenging target for surveys not suited for high precision photometry. The gravitational strain of this system, of  $h \approx 10^{-22}$  is too weak to be detectable by, e.g., LISA.

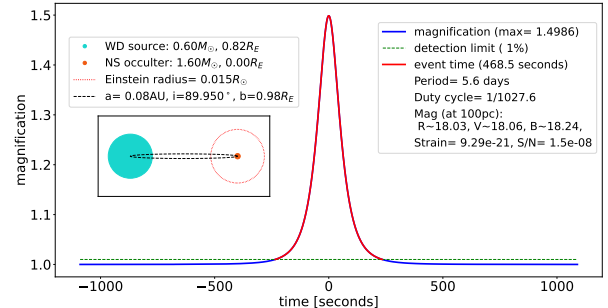


**Figure 8.** A simulated WD-NS system. The plot is similar to Figure 6 but with a NS lensing a WD. The masses of the stars are 0.6 and  $1.6 M_\odot$ . In this example, there is no eclipse, as the size of the NS (on the order of a few km) is negligible when compared to the size of the WD (on the order of thousands of km). The orbital radius is 0.08 AU, giving a 5.6 day orbit. The flare duration is about 500 s, with a duty cycle of about 1/1000. The maximum magnification of 1.5, along with the flare duration, makes this an easy target to detect. Since NSs are more massive and do not create eclipses, they can be detected at lower separations. Thus, there may be detectable WD-NS systems with a substantially higher duty cycle and shorter flare repeat period. The much lower brightness of the NS also means there is no visible lensing when the WD moves in front of the NS. The gravitational strain of this system, of  $h \approx 10^{-22}$  is too weak to be detectable by, e.g., LISA.

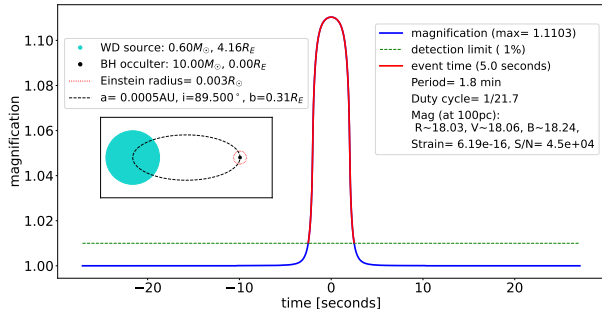


**Figure 9.** A simulated WD-BH system. The plot is similar to Figure 6 but with a BH lensing a WD. The masses of the stars are 0.6 and  $10.0 M_{\odot}$ . In this case, similar to the previous example, there is no eclipse. The high mass of the lens makes it possible to detect flares at lower orbital radius and inclination values. The orbit is only  $5 \times 10^{-4}$  AU, giving a 1.8 minute period. The flare duration is about 5 s, with a duty cycle of about 1/22. The maximum magnification of 1.1, along with the short repeat time, makes this a good target for high cadence surveys. While BHs are expected to be rare, the higher duty cycle, and larger range of inclination angles that are still detectable, might make these sorts of targets favorable despite the presumed lower abundance of systems. The gravitational strain of this system, of  $h \approx 10^{-19}$  is easily detected by a gravitational wave detector like LISA.

tection prospects for various surveys. The biggest considerations are the lens mass and the orbital radius. These determine the Einstein radius which sets the size of the flares. If we assume constant masses for the objects, the semimajor axis, and so the orbital period, determines the flare size. On the other hand, shorter periods are easier to detect, because of the higher duty cycle and larger geometric angle in which lensing can be seen. In Figure 10 we show the magnification as a function of orbital period. The colored curves show WD-WD systems with lensing WDs of different masses. The grey and black curves show a WD with a NS or a BH with lenses of different masses. In all cases the source is a typical WD of  $0.6 M_{\odot}$ .

The WD-WD systems have a sharp drop-off at low periods, which correspond to where the lensing WD starts to also occult the source, which puts them effectively into the regime of eclipsing white dwarfs. This happens at orbital periods of a few hours to close to a year, depending on mass. It should be noted that the majority of eclipsing WDs have been found with considerably shorter periods, owing to the same considerations of duty cycle and geometry that affect self-lensing (Burdge et al. 2019; Coughlin et al. 2020; Burdge et al. 2020).

The WD-NS and WD-BH systems do not show such a drop-off as their physical size is negligible compared to the source size and the Einstein radius. Their flares

are visible above even the higher threshold of 300 mmag down to a period of hours (for the  $1.5 M_{\odot}$  NS) or even minutes (for the  $30 M_{\odot}$  BH).

The text labels on the curves specify the duty cycle for each system as it crosses either the 30 mmag or 300 mmag thresholds. Less massive lenses cross these thresholds at relatively longer periods, corresponding to lower duty cycles. The geometric angle where the flare is visible has a value similar to the duty cycle. Thus an equal mass WD-WD system with  $0.6 M_{\odot}$  (the orange triangles in the figure) can be detected with 300 mmag precision at a period of 12.7 days, with a duty cycle of 1/1620. Thus only one in  $\sim 1600$  systems will have the correct inclination to be visible, and only one in  $\sim 1600$  observations will overlap with the flare time (assuming the exposure time is shorter than the flare duration, which is  $\approx 700$  s in this case). A system with a more massive WD lens with a mass of  $1.2 M_{\odot}$  (the red pentagons in the figure) crosses the 300 mmag threshold at about 1 day, with a duty cycle (and geometric factor) of 1/360. This is still a rare occurrence, and is complicated by the relative scarcity of such heavy WDs. If a population of massive WDs exists but remains undetected due to the objects' smaller size, self lensing would be an excellent way to detect it, if a sufficient number of binary WDs can be observed with sufficient cadence to overcome the 1/360 duty cycle.

For heavier lenses, that also do not eclipse the source, the part of the parameter space that is most interesting for detection is that of minutes to hours periods. Such systems have duty cycles between 1/10 and 1/100 at the periods where they are still above threshold, and any candidate systems found could be followed up easily with a few hours of high cadence imaging. The limiting factor on the intrinsic numbers of these systems comes from the size of the orbits: at orbits shorter than about one minute the WD undergoes Roche-lobe overflow and starts to spill mass unto the lens. For orbits of a few minutes, before mass transfer begins, gravitational wave emission will shrink the orbits and deplete the number of systems available at any given time. Thus, the most viable region of the parameter space to observe NS and BH lenses around a WD, is that of 10–100 minute orbits. The flare durations in such cases are on the order of 10–100 seconds.

## 5. DETECTION PROSPECTS AND SURVEY STRATEGIES

Different surveys have different observing strategies, that can dramatically change the detection prospects for self-lensing events. The most significant parameters for determining the detection rate would be the field



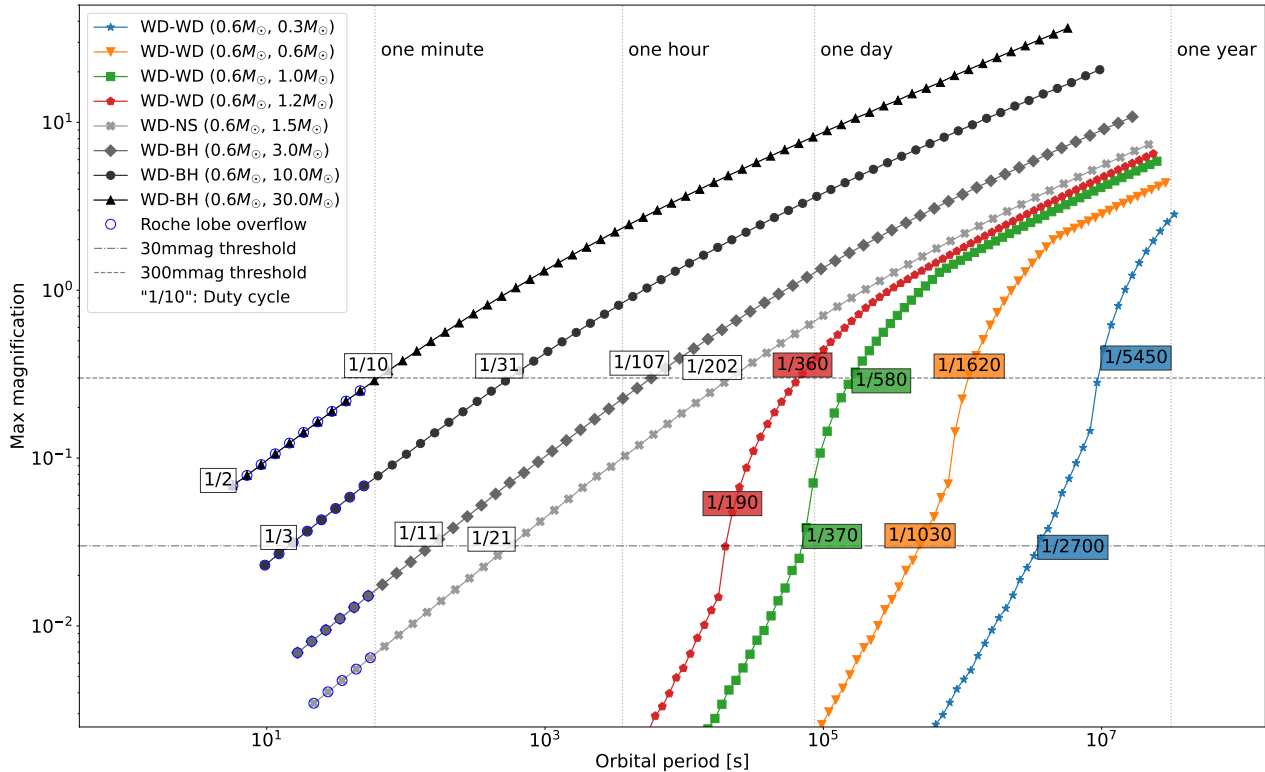


**Figure 10.** Parameter space of self-lensing flares. The magnification vs. orbital period for self-lensing systems with different lens masses. All systems have a source WD with a mass of  $0.6 M_{\odot}$ . The colored curves are for WD-WD systems with masses ranging  $0.3 - 1.2 M_{\odot}$ , while the grey and black curves represent WD-NS and WD-BH systems with masses in the range  $1.5 - 30 M_{\odot}$ . The two dashed, horizontal lines represent 30 and 300 mmag detection thresholds. The text labels show the duty cycle (and are a good approximation for the geometric factor) for each system at the period where it is above each of the thresholds. These numbers give a rough estimate of the number of systems and the number of observations needed per system to see a flare. The blue circles around short period systems represent systems undergoing Roche-lobe overflow.

of view, the depth, the number of visits, and the photometric precision as a function of magnitude. The field of view determines the number of stars that are observed in each visit. Surveys sensitive to fainter objects will also monitor many more stars at higher distances, compared to shallower surveys. For each set of parameters, the probability that the survey observes the system during a flare is proportional to the total amount of time the survey observes each field (i.e., the exposure time multiplied by the number of visits). The third factor, the photometric precision, determines the faintest flares that can be identified by a survey. Fainter flares correspond to systems with closer orbits, that have a higher probability to be seen with the right timing and inclination.

We have chosen to include several surveys that have relatively high cadence, and either a large sky coverage or large depth. This list is not exhaustive but we believe it is representative of some common strategies for existing and planned surveys.

ZTF is a large area, medium depth, all (Northern) sky survey that is focused on finding transients with time scales of days (Bellm et al. 2019). TESS is a satellite mission designed for detecting transits of planets around other stars. It covers the entire sky with long series of observations of 120 s, but has small apertures on its array of four cameras, with a low limiting magnitude and is thus limited to nearby targets (Ricker et al. 2014). LSST is a planned large scale survey of the Southern sky using an unprecedented combination of a large aperture and large field of view, which gives it an advantage in terms of space volume covered (Ivezic et al. 2019). The Dark Energy Camera (DECam; DePoy et al. 2008) has a large aperture but a smaller field of view relative to other surveys we consider. The DECam Deep Drilling Fields (DDF) survey is a 3-night cadence survey with multiple exposures in a series, that may be useful in identifying self-lensing flares (Graham et al. 2023). CuRIOS is a planned array of cubesats that would observe a large fraction of the sky continuously on minutes

time-scales, to a depth substantially larger than that of TESS, and could prove effective in detecting and identifying self-lensing flares (Lu et al. 2022). Finally, LAST is a ground array of small aperture telescopes that also combines a large field of view with medium depth and repeated exposures on time scales of minutes (Ofek et al. 2023). The key properties of each survey as they relate to finding self-lensing flares are shown in Table 2. Note that for surveys with multiple filters and exposure times we have chosen a representative middle value to use in all simulations (which simplified the process). As we are interested in mean values and rough estimates for the number of detections, the exact response of each filter to each system color is not critical, only the average values. In the table, we spell out the different filters for each survey but highlight the one used in the simulation in bold.

To decide if a survey can detect a certain flare at a given distance we use estimates for the precision of each survey as a function of apparent magnitude. The photometric precision used in the simulations for various surveys are shown in Figure 11. The precision values for ZTF are taken from Masci et al. (2019), Figure 9. The precision values for TESS are from a technical note.<sup>3</sup> The precision values for LSST are given in Ivezić et al. (2019), Table 3, multiplying the value in the  $\sigma_1$  column by  $\sqrt{2}$  to convert from two to one exposure of 15 s. We also assume that for stars brighter than 20th magnitude, the single exposure precision never increases above 1.4%. The precision values for DECam are estimated by a noise model with a background count of  $20 \text{ e}^- \text{ s}^{-1}$ , a read noise of  $12 \text{ e}^-$  per exposure, an aperture of 4 m, exposure times of 100 s and a maximum precision of 1%. The precision values for CuRIOS are given by assuming a 15 cm aperture and read-noise of  $\sim 1 \text{ e}^-$  per pixel per frame, based on a preliminary design using the Sony IMS455 sensor (private communication). The precision values for LAST are given by Ofek et al. (2023), Figure 16, blue curve. For stars brighter than 16.5 we assumed the precision does not improve beyond 2% ( $S/N \approx 50$ ).

For surveys that take multiple exposures in a single visit (a photometric series), and for flares that are not shorter than a single exposure, the chances of detecting a flare in each visit would increase compared to the single

<sup>3</sup> <https://heasarc.gsfc.nasa.gov/docs/tess/observing-technical.html>. The precision is adapted by estimating the middle of the distribution of red points, scaled down from 1-hour exposures by  $\sqrt{60/2}$  as an estimate for the precision at 2 minute exposure time.

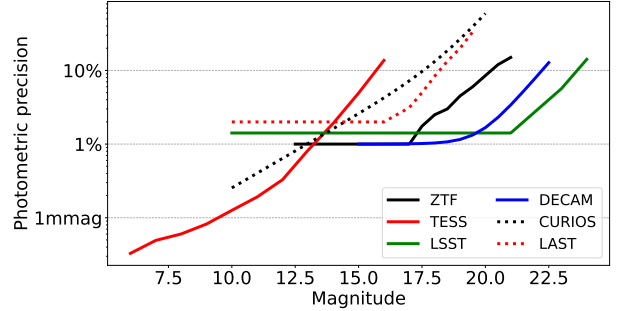


**Figure 11.** Photometric precision of various surveys used in the simulations, as a function of the magnitude of observed objects.

epoch detection, as S/N can be accumulated from multiple images. If the series is longer than the entire period of the system, there could be multiple flares detected consecutively. Such detections would make it much easier to identify the flare is periodic, but we do not address this in the current set of simulations, only the chance to detect a flare in general.

These considerations illustrate that it is not trivial to estimate the detection rate, unless considering all the properties of the survey and the individual lensing system. Thus, we calculate the mean probability for detecting each system, under the observing parameters of each survey, for various distances (in logarithmic steps). The distance to the system determines its apparent magnitude which sets the photometric precision. We test further distances until the system moves below the detection threshold (fainter than the limiting magnitude).

For each system, survey and distance, the detection probability for a single visit  $P_{\text{visit}}$  is calculated. We calculate from that the total probability to detect a flare in a single field  $P_{\text{field}}$  after a number of visits,  $N_{\text{visits}}$ , which is the average number of times each field is observed over the life of the survey. The probability per field is then given by

$$P_{\text{field}} = 1 - (1 - P_{\text{visit}})^{N_{\text{visits}}}. \quad (8)$$

This probability, which is a function of distance, is multiplied by the volume spanned by the field of view area of all the fields in the survey, times the difference in distances. This defines an *effective volume* for the survey:

$$V_{\text{effective}} = N_{\text{fields}} \sum_{r=r_{\text{min}}}^{r_{\text{max}}} P_{\text{field}} \Delta r, \quad (9)$$

where the distance  $r$  takes values starting from 3 pc up to the maximum distance that allows the system to be observed. Multiplying the effective volume by the expected space density of such systems, including random inclinations, gives an estimate of the event rate.

**Table 2.** Survey parameters

Name	Exp. time (seconds)	Series length	Field of view (deg <sup>2</sup> )	Aperture (meters)	Lim. mag.	Filters	phot. prec. (percent)	Duty cycle (percent)
TESS	120	$\sim 10^5$	$4 \times 24$	0.1	16	broadband	0.1–10%	$\sim 100\%$
ZTF	30	1	37	1.2	21	<b>g, r, i</b>	1–1%	$\sim 25\%$
LSST	15	2	10	8.0	24	<b>u, g, r, i, z, y</b>	1–10%	$\sim 25\%$
DECam DDF	100	15	3	4.0	23	<b>g, r, i</b>	1–10%	$\sim 25\%$
CuRIOS	30	30	10	0.1	20	<b>r</b>	0.5–20%	$\sim 100\%$
LAST	15	20	$36 \times 7.4$	0.28	20	broadband	2–15%	$\sim 25\%$

NOTE—Different surveys used in the simulations. To simplify calculations, and get a rough estimate for the number of detections in each survey, we used only a single filter in the simulations. We adopted the cadence of all filters combined, under the assumption that a detection in any filter can be later followed up as a candidate self-lensing flares. E.g., if ZTF takes two images in  $r$  and  $g$  in one night, our simulations will assume two images were taken in  $r$ , when calculating the cadence and detection probabilities. The filter used in the simulation is highlighted in bold in the table. The duty cycle for ground based observatories accounts for loss of observations due to daylight, bad weather, and assumes an average of 6h per night of useful observations.

It is also possible to find the single-visit detection probability for specific object parameters, and compare that with systems that have already been observed, where the distance and some physical properties are known. This can be used to place limits on the presence of unseen companions.

The single visit detection probability is a key metric that must be estimated for each system, survey, and distance. Once the system parameters are determined, we can calculate the flare shape and intensity, and apply each survey to the same flare in turn. For each survey, the combination of precision, exposure time, number of images per visits (series length) and detector dead time is different, and yields a different signal when applied to each flare.

If the flare duration is much shorter than the exposure time ( $t_{\text{flare}} < 0.1t_{\text{exp}}$ ), the signal is given by the average flare intensity, over the exposure time. We calculate the signal-to-noise ratio (S/N) by dividing the signal with the noise level  $\sigma_p$  (equivalent to the photometric precision) at each distance.

$$\text{S/N} = \frac{\int f(t)dt}{t_{\text{exp}}\sigma_p}, \quad (10)$$

where  $f(t) \equiv M(t) - 1$  is the flare flux above the constant star light, given by the magnification  $M(t)$  minus one. Both  $f(t)$  and  $\sigma_p$  are relative to the constant star’s flux.

If the exposure time is not much longer than the flare, we apply a sliding window approach to finding the S/N. We build a uniform window spanning the exposure time, and convolve that with the lightcurve:

$$\text{S/N}(t) = \frac{1}{\sigma_p}(H \star f)(t) = \frac{1}{\sigma_p} \int H(t-t')f(t')dt', \quad (11)$$

where  $\square \star \square$  is the convolution operator, and  $H(t)$  is the “hat function” defined by

$$H(t) = \begin{cases} 1/t_{\text{exp}} & -\frac{1}{2}t_{\text{exp}} < t < \frac{1}{2}t_{\text{exp}} \\ 0 & \text{otherwise.} \end{cases} \quad (12)$$

This takes into consideration all possible time offsets between the exposure and the flare, and produces different values of S/N when integrating different parts of the flare.

This result is for a single exposure. If the series is longer than that, we shift the resulting S/N( $t$ ) function in time by intervals of  $\Delta t = t_{\text{exp}} + t_{\text{dead}}$  and add the results from one exposure to the other in quadrature,

$$\text{S/N}_{\text{total}} = [\text{S/N}(t)^2 + \text{S/N}(t + \Delta t)^2 + \text{S/N}(t + 2\Delta t)^2 + \dots]^{1/2}. \quad (13)$$

This accounts for multiple exposures spanning a single flare, applying a matched-filter approach to adding the S/N from separate exposures.

To convert the S/N into a detection probability, we assume the noise in each exposure is normally distributed, and find the probability of each S/N value of being detected above a pre-defined threshold of  $\tau = 5$ :

$$P_{\text{flare}} = \frac{1}{2} [1 + \text{Er}(\text{S/N} - \tau)], \quad (14)$$

using the error function:

$$\text{Er}(z) = \frac{2}{\pi} \int_0^z e^{-x^2} dx. \quad (15)$$

For  $S/N \ll \tau$  the probability is negligible, while for  $S/N \gg \tau$  the probability approaches 1, which happens for bright flares. For  $S/N \sim \tau$  we get the probability to detect such a flare, with a  $S/N$  that fluctuates with a normal noise with standard deviation of one.

When the  $S/N$  is time-dependent, e.g., Equation 11, we calculate the probability for each time bin of  $S/N(t)$ , and average over the entire period to find the total probability assuming the phase of the orbit is uniformly distributed relative to the time of the exposure/series.

If a single visit with multiple exposures is long enough to observe multiple flares, we calculate the probability to have  $N_{\text{flares}}$  in the series. For each system this spans two numbers, offset by one flare. The probability to detect any flares is:

$$P_{\text{multi flare}} = 1 - (1 - P_{\text{flare}})^{N_{\text{flare}}}, \quad (16)$$

and the total visit probability is the weighted sum of the results for the two possible number of flares.

## 6. RESULTS

One way to summarize the results of each survey over many different self-lensing systems is to calculate the effective volume given some set of system parameters. The effective volume is the product of the space volume observed (the field of view, multiplied by the distance range where the systems were placed in the simulation) with the probability to detect a single flare from such a system over the life-time of the survey. Our simulations assume all surveys observe for 5 years, which is representative of the example surveys we used and allows us to compare each survey's yield per unit time.

The effective volume is necessarily a function of all the system parameters, but we are mostly interested in the marginalized effective volume, where we choose some reasonable values for the distribution of WDs, NSs and BHs, and calculate the mean effective volume for those systems.

The inclination of different systems is uniform in  $\cos i$ , due to the geometry of binaries and is model-independent. The WD masses are chosen using a Gaussian distribution centered on  $\mu_{M_{WD}} = 0.6$ , with a standard deviation of  $\sigma_{M_{WD}} = 0.2$ , both in units of Solar mass. For WD-WD models we use the same mass distribution for both source and lens. The temperatures of the WDs are chosen from a power-law distribution with an index of  $q_{T_{WD}} = -2$ . For NSs and BHs we assume a power law distribution of masses with an index  $q_{M_{BH}} = -2.3$ . We will later show how the results change when modifying this value.

We present the effective volume for WD-WD pairs in Figure 12. Each survey has slightly different effective

volume curves, depending on the exact survey strategy, depth and cadence. We also show as a dashed line the estimated density of binary WDs in our Solar neighborhood (Maoz et al. 2018). The normalization for WD-WD binaries is  $5.5 \times 10^{-4} \text{pc}^{-3}$  (or one system per  $1818 \text{pc}^3$ ). From this plot it is evident that large surveys like LSST, or a large array of space telescopes like the full CuRIOS array, have a volume coverage that easily surpasses the density of WD binaries. Other surveys like ZTF are not designed to detect self-lensing binaries, that have a low duty cycle and often very faint flares, but still have a chance to see a few flares over their lifespan due to their large field of view. However, it should be noted that an array of smaller telescopes like LAST (with much lower construction costs) could have similar performance in terms of finding self-lensing flares, and due to their multiple-image-per-visit strategy, stand a much better chance at identifying the flares. While TESS has good precision and cadence, it does not have the depth required to see many WDs over the entire sky. The DDF survey of DECam, on the other hand, has substantial depth and good cadence, but the small field of view makes it unlikely that any lensing WDs exist in its footprint. It should be noted that even though the effective volume curves of some surveys are below the model density, the integral over all semimajor axis bins can still yield more than a single detection over the life of the survey (as discussed below).

For WDs in binaries with NSs or BHs we have only rough estimates for the intrinsic density of systems in the Solar neighborhood. While population synthesis models exist (e.g., Wiktorowicz et al. 2019; Lam et al. 2020), we choose to simply present a rough estimate based on a reasonable density value, with the understanding that the total number of detections will scale linearly with the density normalization. In Figure 13 we show the effective volume compared to a distribution of NS/BH objects with the same semimajor axis distribution as in Figure 12, but for more massive objects, with masses distributed according to a power law with an index of  $-2.3$ . This plot shows that, as before, a deep survey like LSST, or a shallow survey with all-sky coverage like CuRIOS (full array) will have dramatically better chances of seeing self-lensing flares than other surveys in our simulations. Note that the range of semimajor axes, and so the orbital periods, spans much shorter values in this figure.

The corresponding flare durations of seconds to minutes may make it very hard to identify the flares are astrophysical, rather than instrumental or coming from some foreground effects, when they are seen in only one, isolated exposure. Furthermore, care should be



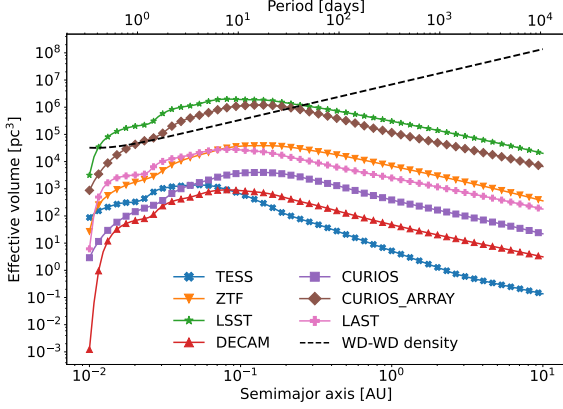


**Figure 12.** Effective volume for detecting WD-WD binaries using different surveys. The dashed line represents an estimate for the space density of double white dwarfs of one double WD (DWD) per  $1818 \text{ pc}^3$  (Maoz et al. 2018). We can see the great depth and substantial field of view of LSST give it a clear advantage in detecting self-lensing flares, with the (substantially less expensive) array of CuRIOS satellites getting very similar results based on their all-sky coverage. Two other noteworthy surveys are ZTF and the-soon-to-be-operational LAST, that may also provide some detections over their life-spans. The single CuRIOS, TESS and DECAM all have insufficient depth or coverage to detect meaningful number of WD-WD self-lensing pairs.

taken when considering the semimajor axis distribution of massive compact objects. While we do not know the shape of the orbital distribution (or overall normalization) of WD-NS or WD-BH binaries, we can use this rough estimate to show what regions of the semimajor-axis parameter range are most likely to provide detections. Since the semimajor axis distribution is based on an initial power law, modified by gravitational wave emission (Maoz et al. 2018), the overall shape should be similar to the WD-WD case, although we note that the initial power law index is unknown for NSs/BHs and is copied from the WD case as a placeholder, as is the arbitrary normalization of  $10^{-5}$  systems per  $\text{pc}^3$  (including WD-NS and WD-BH systems on a single mass spectrum with a single power law).

To estimate the total number of detections in each survey we must integrate the product of the effective volume with the probability to find each parameter:

$$N_{\text{total}} = \int V(\Theta)P(\Theta)d\Theta, \quad (17)$$

where the effective volume  $V$  and the probability to find a system  $P$  are both functions of the set of parameters  $\Theta$  that include the masses, temperatures, inclination and semimajor-axis of each system. In the case of DWDs, the space density and distributions of mass, temperature and separation are relatively well known (e.g., Maoz

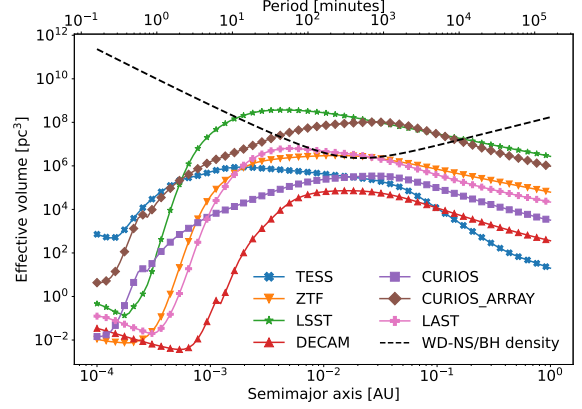


**Figure 13.** Effective volume for detecting WD-NS/BH binaries using different surveys. The dashed line uses the same semimajor-axis distribution as in Figure 12 from Maoz et al. (2018), adapted for higher-mass objects such as NSs and BHs. The overall normalization of  $10^{-5}$  per  $\text{pc}^3$  is arbitrarily chosen, as is the initial semimajor axis power law index and the mass power law index (see text). Here, too, we see that LSST, with its superior depth, and CuRIOS (full array), with its high cadence and sky coverage, have superior detection prospects relative to the other surveys.

et al. 2018), so we use those estimates to get a rough number of detection in each survey.

For NSs and BHs in binaries with WDs, the numbers are essentially unknown, and can currently be estimated only using population synthesis codes. We will simplify the process by plugging in some range of reasonable distributions, to see how much the results change. The critical missing value, obviously, is the total number density of WD-NS or WD-BH pairs in the solar neighborhood. We will assume this number (over all masses and separations) is simply given as one system per  $10^5 \text{ pc}^3$ , and caution that the numbers we get based on this assumption should be rescaled to more realistic numbers using, e.g., population synthesis codes. The results are summarized in Table 3. The exact choice of power law index for the mass of NS/BH companions changes the resulting number of detections by up to  $\pm 20\%$ , but given the uncertainties in the overall normalization (the total number density of WD-NS and WD-BH pairs) is probably not the main cause for uncertainty.

While some of the detection numbers in Table 3 may seem high, we caution that some of the systems we discuss will have a long period (of years) and would be very hard to follow up. To get a rough estimate for how many systems we would actually be able to identify, we calculate the probability of each system to be identifiable in a dedicated followup campaign. As an example, we will assume a dedicated telescope will spend an average 2.4

**Table 3.** Expected number of detections

Survey	WD-WD	WD-NS/BH		
		low	mid	high
TESS	0.3	2.2	2.5	2.8
ZTF	3.3	18.0	21.3	24.7
LSST	246.8	1314.8	1466.1	1614.5
DECAM	0.1	0.4	0.5	0.6
CURIOS	0.3	2.0	2.5	3.0
CURIOS_ARRAY	93.1	586.2	742.1	907.5
LAST	3.7	23.6	26.9	30.3

NOTE—The low, mid and high columns correspond to power law indices for the NS/BH mass distribution. In the simulations we used  $-2.7$ ,  $-2.3$  and  $-2.0$  as the indices for the low, mid and high, respectively. The larger (less negative) index implies more BHs with higher mass, which increases the number of detections. The total number density for WD-WD pairs is taken to be one system in  $1818 \text{ pc}^3$  (Maoz et al. 2018). We assumed the total number density of all binaries of a WD with a NS/BH companion (with  $M > 1.5 M_{\odot}$ ) are one system per  $10^5 \text{ pc}^3$ . This density is only given as a placeholder, to be rescaled with the expected real number density from, e.g., population synthesis codes.

hours each night following up a WD that had displayed a flare, over a whole year. The probability to see a flare during that time is:

$$P_{\text{followup}} = 1 - (1 - f)^N, \quad (18)$$

where  $f = 0.1$  is the fraction of time the target is observed, and  $N = \lfloor T_{\text{followup}}/T_{\text{orbit}} \rfloor$ , with  $T_{\text{followup}} = 1 \text{ yr}$  and  $T_{\text{orbit}}$  being the orbital period. Note that systems with  $T_{\text{orbit}} > T_{\text{followup}}$  will not be included in the total effective volume and will not contribute to the total number of detections. Of course, followup could be distributed to multiple telescopes around the world, raising  $f$  towards unity; On the other hand, many candidates would need to be followed up simultaneously, reducing the time a telescope can observe each target to a few minutes per night, such that  $f$  could also be much smaller; and clearly, the limit of one year is arbitrarily chosen. These parameters are used to estimate how the total number of detections would be limited by the requirement that systems are within reasonable possibility of a followup campaign.

In Figure 14 we show the number of detections (the product of the effective volume and the assumed number density of systems) as a function of semimajor axis for WD-WD systems (left panel) and for WD-NS/BH sys-

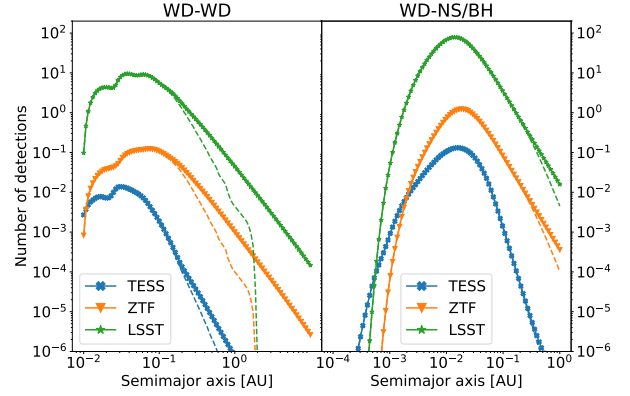


**Figure 14.** The number of WD-WD (left) and WD-NS/BH (right) detections as a function of semimajor axis for three representative surveys. The dashed lines represent the number of detected flares that could reasonably be followed up within a year of 10% observing fraction (see text). The effect of a year of followup are more substantial for the WD-WD case, where the orbits are wider. It should be noted that if the followup campaign is shorter than a year (e.g., due to funding or sun angle constraints) the effects would be felt at closer orbits.

tems (right panel). Note the two panels use a different range of semimajor axis values. The overall normalization of the detection curves depends on the semimajor axis bin size, and should be integrated over all bins to get the total number of detections, as shown in Table 3. However, the shape of these curves also help guide surveys to look for each type of system at the optimal range of orbital periods for detection. Since the assumed distributions of compact binaries as a function of semimajor axis have a peak that partially overlaps with the peak in effective volume (see Figures 12 and 13), the shape of the expected detections curves is qualitatively similar to the effective volume curves. The dashed lines in Figure 14 show the number of detections that can also be identified using the followup campaign described by Equation 18. The WD-WD systems are more affected by this requirement, as they generally need wider orbits to be detectable. The chosen followup campaign parameters give a gradual decline starting at orbits of a few weeks, and a sharp drop-off at one-year orbits. This does not affect the peak of the distribution that occurs for most surveys around 10 days. However, shorter followup campaigns (due to, e.g., funding limits or sun-angle constraints) would shift this decline in numbers to shorter periods, and could impact the chances of detecting and identifying self-lensing flares.

To get a sense of how that total number of detections would change using different mass distribution models for NS/BH lenses, we integrate the effective volume mul-

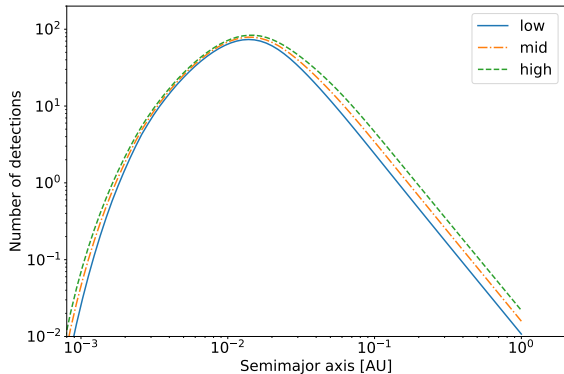


**Figure 15.** The number of WD-NS/BH detections as a function of semimajor axis for the LSST survey, based on different choices of mass power law index. The total number of detections changes by up to a factor of 2, but the overall shape of the curve does not change dramatically. The index choices used in this work are  $-2.7$ ,  $-2.3$  and  $-2.0$ , for the low, mid and high mass distributions, respectively.

multiplied by different probability functions for the mass of the lens in each binary system. Besides the model already presented in previous figures (using an index of  $-2.3$ ), we also use a “low” and “high” indices of  $-2.7$  and  $-2.0$ , respectively. The model with the less negative value (the “high” model) has more black holes with a high mass, that are generally easier to detect. We show the number of WD-NS/BH detections expected for LSST, using different power law indices in Figure 15. We see that the numbers change by up to a factor of 2 at some range of semimajor axis values, but we also note that when integrating all the detections we are left with a difference of about 20% in either direction from the “mid” distribution (as seen in Table 3).

To further explore the way our results would change under arbitrary choices of mass distributions<sup>4</sup> we show the effective volume of WD-NS/BH systems as a function of lens mass, this time marginalizing over the semimajor axis distribution (we use the same distribution used above for modeling the WD-NS/BH population). We show the results, for three representative surveys, in Figure 16.

For each survey we attempt to fit the effective volume curve using a linear function of the lens mass,  $M_L$ . At low masses, it seems the effective volume increases quickly on a curved slope, presumably due to the increased parameter space at closer orbits that becomes

<sup>4</sup> E.g., a realistic mass distribution that has a different shape for NSs and for BHs, that would presumably arise from different processes of stellar deaths that produce NSs vs. BHs.

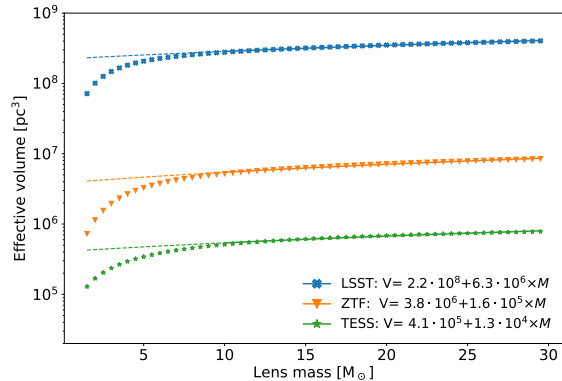


**Figure 16.** The effective volume of WD-NS/BH detections as a function of mass for three representative surveys. The semimajor axis has been marginalized over using the same distribution shown as a dashed line in Figure 13. We fit a linear function to each curve, using only values of  $M_L > 10 M_\odot$ , where the effective volume grows linearly with mass (solid curve). The dashed curve shows the extrapolation of the linear function, to regions where the effective volume grows faster with the lens mass than the fitted linear function.

available as the mass increases and the flares become detectable at shorter orbits. At high mass values we expect that the Einstein radius will increase as  $\sqrt{M_L}$  (see Equation 2, which contributes to increasing the geometric factor and the duty cycle. Together, the effective volume increases as a linear function of mass. To fit this behavior, we used only effective volume values where  $M_L > 10 M_\odot$  to find the parameters of the linear function (the solid line represents the area used in the fit, while the dashed line shows the continuation of the line down to the region where the effective volume is non-linear with lens mass).

## 7. DISCUSSION

Detecting WD-WD self-lensing binaries is difficult. The requirement for the lensing to overcome the physical eclipse means that only pairs with relatively wide orbits can be detected. Eclipsing WD-WD binaries, on the other hand, with shorter orbits of minutes up to about an hour, are easier to detect due to their higher geometric factor and duty cycle. Even though the intrinsic density of DWDs decreases with orbits shorter than the peak (around one day orbits), the prospects for detecting the minute to hour eclipsing binaries would be higher. The fact that with closer orbits the physical size of the eclipsing WD does not shrink (as does the Einstein radius) means that the detection probability will scale with  $a^{-2}$ , instead of  $a^{-1}$  that is typical of self lensing events.

Indeed, cases of successful identification of WD-WD eclipsing binaries in archival ZTF data have been reported (Burdge et al. 2019; Coughlin et al. 2020; Burdige et al. 2020). In these cases, the short orbital periods and associated high duty cycle benefited from a folding analysis that combined the S/N from multiple eclipses that allowed detection of fainter signals than what would be possible using individual eclipses. Considering that self-lensing flares would only be detectable, for WD binaries, with orbital periods of  $\sim 1$  day, it is reasonable to expect an order of magnitude fewer detections of self-lensing flares in the entire ZTF archive. These longer orbits would also make it very unlikely to see more than one flare per system, so a search based on folding all epochs in the archive over different test periods would most likely not improve the detection prospects.

Our results for ZTF (in Table 3) estimate that there should be around three flares detected from three separate WDs during five years of ZTF operations. This is roughly consistent with the number of eclipsing WDs in the ZTF archive. As we would expect an order of magnitude less self-lensing DWDs to be detectable in the same dataset, the estimates given by our simulations are perhaps somewhat optimistic. Searching for such flares in archival ZTF data is underway.

WDs in close binaries with NSs or BHs would not have any detectable eclipses, and can be seen only by light-curve variability caused by elliptical modulations, Doppler beaming or self lensing (Masuda & Hotokezaka 2019; Chawla et al. 2023). The shorter periods and higher geometric factors and duty cycles relevant for detection of these more massive objects should yield more detections, provided the underlying number of systems is high enough. Searches already conducted for eclipsing DWDs in ZTF data had not led to the discovery of any WD-NS or WD-BH self-lensing flares. This may be an indication that the number density of such systems is lower (by an order of magnitude or more) than the placeholder value of  $10^{-5} \text{ pc}^{-3}$  we used to produce the values in Table 3.

Considering, instead, the detection prospects for a survey such as TESS, we may start by assessing the number of available WDs that are observable with sufficient photometric precision. Using the WD catalog assembled by Gentile Fusillo et al. (2021), we find a total of 4125 WDs brighter than  $G < 16$ , or  $\approx 33000$  WDs brighter than  $G < 18$  (magnitudes given by the Gaia  $G$  band). Since DWDs constitute about 10% of the total WD population, and since the geometric factor for self-lensing systems with the appropriate  $\sim 1$  day orbit is  $\approx 1/1000$ , we would expect less than one detection in the  $G < 16$  census of WDs that may be bright enough to be successfully

monitored by TESS. This back-of-the-envelope calculation is consistent with our simulation results. However, a search for faint, symmetrical flares using a matched-filter approach (Turin 1960), perhaps also using folding on a range of trial periods may be warranted, to verify that an unknown population of DWDs is not hiding in the data.

How would our results change if we considered main sequence stars instead of WDs as the sources that are being lensed? While a detailed analysis with a full simulation set is reserved to future work (and has already been considered elsewhere Agol 2003; Rahvar et al. 2011; Wiktorowicz et al. 2021), we can make some general remarks based on scaling the current results.

A main sequence star like our sun, is about 100 times the radius of a typical WD. Even if we consider smaller stars, the sources will be larger and the flares more diluted, unless the orbits are also substantially larger. To preserve the same ratio of the Einstein radius to the source radius, for a star  $X$  times larger than the typical WD, would require an orbit with a semimajor axis that is  $X^2$  larger (see Equation 2). This leads to an increase of orbital period of  $X^3$ . Thus, a one-day DWD binary will have a similar flare magnitude as a 1000-day M-dwarf-WD binary, assuming the M-dwarf is just 10 times larger than the WD. The overall phase space (geometric factor times the duty cycle) scales as  $a^{-1}$  so the number of detectable flares would shrink as  $X^{-2}$  when considering these larger sources. It should be noted that surveys with substantially better photometric precision can be sensitive to shorter orbit MS-WD binaries, as indeed was the case for five different systems found in the Kepler footprint (Kruse & Agol 2014; Kawahara et al. 2018; Masuda et al. 2019).

The reduced probability to see a flaring MS-WD system with a wider orbit does not mean that such systems will be harder to find. WDs are a small population and are much fainter than MS stars. Under the simplifying assumption that the total number density of DWD systems is the same as that of our hypothetical MS-WD systems where the MS star's radius is  $X$  times the radius of the WD, the distance at which our MS systems are visible in space grows also as  $X$  (under the wrong assumption of equal temperature). Under all these overly simplistic assumptions, the factor of  $X^3$  increase in MS-WD systems caused by the larger accessible space volume compensates for the lower geometric factor and duty cycle of the larger orbits (which scales as  $X^{-2}$  as mentioned above). Obviously, the exact distribution of stellar sizes and temperatures should be used to calculate the expected number of detections, using similar methods to those presented in this work.



Even with such simple assumptions, it is plausible that there would be no shortage of wide-orbit, MS-WD systems that can be detected with the same  $\sim 1\%$  precision characteristic of most ground based telescopes.

However, the fact that such events would have a repeat period of  $\approx 1000$  days even for  $X \approx 10$  means that any such systems that are detected would be very difficult to follow up. A survey like LSST, which stands a good chance of detecting many such flares in a single visit (of one 30s exposure or two 15s exposures) over the survey lifespan, would not have any simple way to differentiate the flare from a stellar eruption or other types of artefacts like satellites or cosmic rays.

The results for WD-NS and WD-BH systems are heavily model-dependent. Since there are no direct measurements of populations of WDs in binaries with heavier compact objects, we are left with population synthesis codes. While we do not expect the (probably optimistic) numbers in Table 3 to reflect the actual numbers that would be detected, the converse may become true: with continued observations and sufficient, dedicated photometric followup campaigns, we stand a good chance of constraining this unknown population of massive, compact objects based on detection (or lack thereof) of self-lensing flares.

The parameter space for detecting these more massive binaries is not constrained by eclipses, so that much shorter orbits are still viable targets for ground based surveys. For the relatively wider orbits required for detecting MS stars in binaries with NSs or BHs the parameter space is also still viable. Where a WD-BH system would be most likely detected at minutes-hours orbits (see Figure 10) replacing the WD with a small MS star increases the relevant orbits to the few-day period range, which is still accessible to followup with relatively minor investment of resources.

In all the cases discussed above, whether the source is a WD or a MS star, and in all but the shortest orbits where BH companions could conceivably be detected, the expected flares would present as a symmetric signal over minutes or hours. This raises the importance of surveys that employ long visits of consecutive exposures on the same field. Not only would such strategy help rule out asteroids, satellites and cosmic rays, when multiple exposures show the signal appear and fade away, but having additional information on the shape of the light-curve would be pivotal in identifying the best candidates for self lensing.

Another way to distinguish self-lensing flares would be by simultaneously observing in multiple filters. Up to corrections due to limb-darkening, self-lensing flares

will be achromatic, while stellar flares are expected to be blue.

These observing strategies are especially important for detecting flares from MS sources, particularly from smaller, late type stars, as they will inevitably suffer from a background of stellar flares that could have similar time-scales to self-lensing flares, but with very different spectra and morphology (Kulkarni & Rau 2006).

## 8. CONCLUSIONS

We present a simulation tool to efficiently reproduce light-curves of self-lensing flares in a wide range of system parameters.<sup>5</sup> In addition, the tools we developed include methods for simulating sky surveys with various strategies, allowing a calculation of the expected number of detections for different populations of self-lensing binaries.

Using these tools we map the parameter space of self-lensing system and provide some estimates for ranges of parameters that are most relevant for detecting either WD-WD systems or WD-NS and WD-BH systems, that are qualitatively different as the former is affected by eclipses while the latter is more massive and has negligible eclipses. A major result of this work is given in Figure 10, which is a map for the complicated landscape describing the detection prospects of different systems. The interplay of photometric precision, orbital period and duty cycle (which is also a good estimate for the geometric factor) are mapped out for future surveys searching for self-lensing flares.

We presented a few example surveys that show how different strategies could be more or less effective in detecting self-lensing flares. Notably, the LSST survey dominates the detection potential due to its formidable combination of depth, field of view and cadence. However, we caution that even with the potential to detect hundreds of flares, it is not certain that such a survey will be able to differentiate self-lensing flares from other fast transients and artefacts. On the contrary, an array of small satellites dedicated to high-precision photometry of a large fraction of the sky (e.g., the planned CuRIOS array) can provide a similar yield of detected flares, but with a much denser cadence that would make it much easier to identify the nature of the flares. The lower depth of such a mission also allows cross-matching to other catalogs and identifying the sources of flares as being small stars or WDs (e.g., using Gaia, as in the case for identifying WDs; Gentile Fusillo et al. 2021).

<sup>5</sup> [https://github.com/guynir42/self\\_lens](https://github.com/guynir42/self_lens)

Another survey we considered was ZTF. Despite being designed to detect slower transients on timescales of days and weeks, ZTF still has some potential for detecting self-lensing flares. Efforts to scan archival data for flare-like events from WD source is underway. However, we caution that the lower cadence will likely not allow detection of the same source with multiple exposures, so here, too, identification of self lensing would be difficult. With a handful of eclipsing DWD systems already detected by ZTF, a comparison of the detection prospects for self-lensing flares is consistent with having a between zero to a few detections over the lifespan of the survey. A survey with similar grasp to ZTF that is currently under commissioning is LAST, which has similar detection statistics but has the advantage of making visits of multiple exposures in a single field, which, again, is instrumental in identifying candidates for self lensing.

We expect fewer than one DWD self-lensing flare to be detected in TESS data. The limiting factor in this case is the shallow depth that is accessible to the survey, yielding a relatively small number of WDs to monitor.

Finally, we discuss the detection prospects of WDs in binaries with NSs and BHs. Our results are fairly robust in terms of the range of orbital periods that are most likely to be detectable, and refer again to the map of the parameter space in Figure 10. We caution, however, that the underlying population of such binaries is essentially unknown, and even with sophisticated population synthesis codes, the channels to produce systems with such a large mass-disparity between the binary components are very much model-dependent. And so, admitting our lack of knowledge of the number density (or even existence) of such systems, we provide very rough estimates for the detection prospects in different sur-

veys. On the other hand, (non-) detection of NS/BH self-lensing flares (with WD or MS source stars) could be a promising channel for constraining populations of which we know very little. Surveys such as CuRIOS (and to a lesser degree, LAST) have a suitable visit strategies for detecting and identifying short-lived flares. We argue that an informed search for flares of the appropriate shape, length and periodicity would be a valuable endeavor, that could shed light on an otherwise unknown, dark population.

## 9. DATA AVAILABILITY

The code used to generate all simulations, tables and figures can be found at [https://github.com/guynir42/self\\_lens](https://github.com/guynir42/self_lens)<sup>6</sup>. The source matrices used to speed up simulation times are included in the above code repository and are also available as a Zenodo dataset at <https://zenodo.org/record/8418767>. They can be regenerated locally using the `scripts` folder using a different set of parameters, if needed. The effective volume datasets used as the basis for the results in this work can be simulated using the given code repository, but are also made available through two Zenodo datasets, one for DWD binaries: <https://zenodo.org/record/8340555>; and one for WDs with NS/BH companions: <https://zenodo.org/record/8340930>. These datasets are usually downloaded automatically by the `self lens` package when running the test suite on a local machine.

## 10. ACKNOWLEDGEMENTS

JSB and GN were partially supported by the Gordon and Betty Moore Foundation. We thank N. Abrams, H. Gulick and J. Lu for fruitful discussions of WD-BH populations and the upcoming CuRIOS mission.

## REFERENCES

- Adamane Pallathadka, G., Chandra, V., Zakamska, N. L., et al. 2023, arXiv e-prints, arXiv:2310.16313, doi: [10.48550/arXiv.2310.16313](https://doi.org/10.48550/arXiv.2310.16313)
- Agol, E. 2003, ApJ, 594, 449, doi: [10.1086/376833](https://doi.org/10.1086/376833)
- Bellm, E. C., Kulkarni, S. R., Graham, M. J., et al. 2019, PASP, 131, 018002, doi: [10.1088/1538-3873/aaecbe](https://doi.org/10.1088/1538-3873/aaecbe)
- Bennett, D. P., Becker, A. C., Quinn, J. L., et al. 2002, ApJ, 579, 639, doi: [10.1086/342225](https://doi.org/10.1086/342225)
- Beskin, G. M., & Tuntsov, A. V. 2002, A&A, 394, 489, doi: [10.1051/0004-6361:20021150](https://doi.org/10.1051/0004-6361:20021150)
- Brown, W. R., Kilic, M., Kenyon, S. J., & Gianninas, A. 2016, ApJ, 824, 46, doi: [10.3847/0004-637X/824/1/46](https://doi.org/10.3847/0004-637X/824/1/46)
- Burdge, K. B., Coughlin, M. W., Fuller, J., et al. 2019, Nature, 571, 528, doi: [10.1038/s41586-019-1403-0](https://doi.org/10.1038/s41586-019-1403-0)
- . 2020, ApJL, 905, L7, doi: [10.3847/2041-8213/abca91](https://doi.org/10.3847/2041-8213/abca91)
- Chawla, C., Chatterjee, S., Shah, N., & Breivik, K. 2023, arXiv e-prints, arXiv:2310.16891, doi: [10.48550/arXiv.2310.16891](https://doi.org/10.48550/arXiv.2310.16891)
- Corbett, H., Law, N. M., Soto, A. V., et al. 2020, ApJL, 903, L27, doi: [10.3847/2041-8213/abee5](https://doi.org/10.3847/2041-8213/abee5)
- Coughlin, M. W., Burdge, K., Phinney, E. S., et al. 2020, MNRAS, 494, L91, doi: [10.1093/mnras/rlaa044](https://doi.org/10.1093/mnras/rlaa044)

<sup>6</sup> The precise commit used in this work is at [https://github.com/guynir42/self\\_lens/commit/3977424c6e2944603e7330ebdc2339ebfe5cd95e](https://github.com/guynir42/self_lens/commit/3977424c6e2944603e7330ebdc2339ebfe5cd95e).

- DePoy, D. L., Abbott, T., Annis, J., et al. 2008, in Society of Photo-Optical Instrumentation Engineers (SPIE) Conference Series, Vol. 7014, Ground-based and Airborne Instrumentation for Astronomy II, ed. I. S. McLean & M. M. Casali, 70140E, doi: [10.1117/12.789466](https://doi.org/10.1117/12.789466)
- D’Orazio, D. J., & Di Stefano, R. 2020, MNRAS, 491, 1506, doi: [10.1093/mnras/stz3086](https://doi.org/10.1093/mnras/stz3086)
- Einstein, A. 1936, Science, 84, 506, doi: [10.1126/science.84.2188.506](https://doi.org/10.1126/science.84.2188.506)
- Gentile Fusillo, N. P., Tremblay, P. E., Cukanovaite, E., et al. 2021, MNRAS, 508, 3877, doi: [10.1093/mnras/stab2672](https://doi.org/10.1093/mnras/stab2672)
- Graham, M. L., Knop, R. A., Kennedy, T. D., et al. 2023, MNRAS, 519, 3881, doi: [10.1093/mnras/stac3363](https://doi.org/10.1093/mnras/stac3363)
- Han, C. 2016, ApJ, 820, 53, doi: [10.3847/0004-637X/820/1/53](https://doi.org/10.3847/0004-637X/820/1/53)
- Istrate, A. G., Tauris, T. M., & Langer, N. 2014, A&A, 571, A45, doi: [10.1051/0004-6361/201424680](https://doi.org/10.1051/0004-6361/201424680)
- Ivezic, Z. 2007, in Bulletin of the American Astronomical Society, Vol. 39, American Astronomical Society Meeting Abstracts #210, 174
- Ivezic, Ž., Kahn, S. M., Tyson, J. A., et al. 2019, ApJ, 873, 111, doi: [10.3847/1538-4357/ab042c](https://doi.org/10.3847/1538-4357/ab042c)
- Kasuya, S., Honda, M., & Mishima, R. 2011, MNRAS, 411, 1863, doi: [10.1111/j.1365-2966.2010.17809.x](https://doi.org/10.1111/j.1365-2966.2010.17809.x)
- Kawahara, H., Masuda, K., MacLeod, M., et al. 2018, AJ, 155, 144, doi: [10.3847/1538-3881/aaaaaf](https://doi.org/10.3847/1538-3881/aaaaaf)
- Kruse, E., & Agol, E. 2014, Science, 344, 275, doi: [10.1126/science.1251999](https://doi.org/10.1126/science.1251999)
- Kulkarni, S. R., & Rau, A. 2006, ApJL, 644, L63, doi: [10.1086/505423](https://doi.org/10.1086/505423)
- Lam, C. Y., Lu, J. R., Hosek, Matthew W., J., Dawson, W. A., & Golovich, N. R. 2020, ApJ, 889, 31, doi: [10.3847/1538-4357/ab5fd3](https://doi.org/10.3847/1538-4357/ab5fd3)
- Lam, C. Y., Lu, J. R., Udalski, A., et al. 2022, ApJL, 933, L23, doi: [10.3847/2041-8213/ac7442](https://doi.org/10.3847/2041-8213/ac7442)
- Law, N. M., Corbett, H., Galliher, N. W., et al. 2022, PASP, 134, 035003, doi: [10.1088/1538-3873/ac4811](https://doi.org/10.1088/1538-3873/ac4811)
- Lu, J. R., Gulick, H., Beckwith, S., Bloom, J., & Nir, G. 2022, in Space Telescopes and Instrumentation 2022: Optical, Infrared, and Millimeter Wave, ed. L. E. Coyle, S. Matsuura, & M. D. Perrin, Vol. 12180, International Society for Optics and Photonics (SPIE), 1218008, doi: [10.1117/12.2630122](https://doi.org/10.1117/12.2630122)
- Maeder, A. 1973, A&A, 26, 215
- Maoz, D., Hallakoun, N., & Badenes, C. 2018, MNRAS, 476, 2584, doi: [10.1093/mnras/sty339](https://doi.org/10.1093/mnras/sty339)
- Masci, F. J., Laher, R. R., Rusholme, B., et al. 2019, PASP, 131, 018003, doi: [10.1088/1538-3873/aae8ac](https://doi.org/10.1088/1538-3873/aae8ac)
- Masuda, K., & Hotokezaka, K. 2019, ApJ, 883, 169, doi: [10.3847/1538-4357/ab3a4f](https://doi.org/10.3847/1538-4357/ab3a4f)
- Masuda, K., Kawahara, H., Latham, D. W., et al. 2019, ApJL, 881, L3, doi: [10.3847/2041-8213/ab321b](https://doi.org/10.3847/2041-8213/ab321b)
- Mróz, P., Udalski, A., Skowron, J., et al. 2019, ApJS, 244, 29, doi: [10.3847/1538-4365/ab426b](https://doi.org/10.3847/1538-4365/ab426b)
- Nauenberg, M. 1972, ApJ, 175, 417, doi: [10.1086/151568](https://doi.org/10.1086/151568)
- Nir, G., Ofek, E. O., Ben-Ami, S., et al. 2021a, MNRAS, 505, 2477, doi: [10.1093/mnras/stab1437](https://doi.org/10.1093/mnras/stab1437)
- . 2021b, PASP, 133, 075002, doi: [10.1088/1538-3873/ac0da0](https://doi.org/10.1088/1538-3873/ac0da0)
- Ofek, E. O., & Ben-Ami, S. 2020, PASP, 132, 125004, doi: [10.1088/1538-3873/abc14c](https://doi.org/10.1088/1538-3873/abc14c)
- Ofek, E. O., Ben-Ami, S., Polishook, D., et al. 2023, PASP, 135, 065001, doi: [10.1088/1538-3873/acd8f0](https://doi.org/10.1088/1538-3873/acd8f0)
- Paczyński, B. 1986, ApJ, 304, 1, doi: [10.1086/164140](https://doi.org/10.1086/164140)
- Qin, B., Wu, X.-p., & Zou, Z.-l. 1997, Chinese Physics Letters, 14, 155, doi: [10.1088/0256-307X/14/2/022](https://doi.org/10.1088/0256-307X/14/2/022)
- Rahvar, S., Mehrabi, A., & Dominik, M. 2011, MNRAS, 410, 912, doi: [10.1111/j.1365-2966.2010.17490.x](https://doi.org/10.1111/j.1365-2966.2010.17490.x)
- Ratzloff, J. K., Law, N. M., Fors, O., et al. 2019, PASP, 131, 075001, doi: [10.1088/1538-3873/ab19d0](https://doi.org/10.1088/1538-3873/ab19d0)
- Refsdal, S. 1964, MNRAS, 128, 295, doi: [10.1093/mnras/128.4.295](https://doi.org/10.1093/mnras/128.4.295)
- Ricker, G. R., Winn, J. N., Vanderspek, R., et al. 2014, in Society of Photo-Optical Instrumentation Engineers (SPIE) Conference Series, Vol. 9143, Proc. SPIE, 914320, doi: [10.1117/12.2063489](https://doi.org/10.1117/12.2063489)
- Rybicki, K. A., Wyrzykowski, L., Klencki, J., et al. 2018, MNRAS, 476, 2013, doi: [10.1093/mnras/sty356](https://doi.org/10.1093/mnras/sty356)
- Shappee, B. J., Prieto, J. L., Grupe, D., et al. 2014, ApJ, 788, 48, doi: [10.1088/0004-637X/788/1/48](https://doi.org/10.1088/0004-637X/788/1/48)
- Smith, T. L., & Caldwell, R. R. 2019, PhRvD, 100, 104055, doi: [10.1103/PhysRevD.100.104055](https://doi.org/10.1103/PhysRevD.100.104055)
- Toonen, S., Hollands, M., Gänsicke, B. T., & Boekholt, T. 2017, A&A, 602, A16, doi: [10.1051/0004-6361/201629978](https://doi.org/10.1051/0004-6361/201629978)
- Turin, G. 1960, IRE Transactions on Information Theory, 6, 311, doi: [10.1109/TIT.1960.1057571](https://doi.org/10.1109/TIT.1960.1057571)
- Wiktorowicz, G., Middleton, M., Khan, N., et al. 2021, MNRAS, 507, 374, doi: [10.1093/mnras/stab2135](https://doi.org/10.1093/mnras/stab2135)
- Wiktorowicz, G., Wyrzykowski, L., Chruslinska, M., et al. 2019, ApJ, 885, 1, doi: [10.3847/1538-4357/ab45e6](https://doi.org/10.3847/1538-4357/ab45e6)
- York, D. G., Adelman, J., Anderson, John E., J., et al. 2000, AJ, 120, 1579, doi: [10.1086/301513](https://doi.org/10.1086/301513)